Journal of
Materials Chemistry A

ROYAL SOCIETY
OF CHEMISTRY

PAPER

View Article Online
View Journal | View Issue

Cite this: *J. Mater. Chem. A*, 2024, **12**, 13446

Binder-free MoSe/MMSe composite and onion-derived activated carbon electrode materials for high-performance hybrid supercapacitors†

Manchi Nagaraju, Bhimanaboina Ramulu, Ampasala Surya Kiran and Jae Su Yu*

Received 15th March 2024
Accepted 24th April 2024

DOI: 10.1039/d4ta01755b

rsc.li/materials-a

Strategies and preparation of innovative novel electrode materials are essential for the supercapacitor (SC) industry to enhance their electrochemical performance and cycling stability. Recently, binary transition metal selenides have attracted considerable interest for SC applications owing to their significant theoretical capacitance, easily tunable nanostructures, low cost, environmental friendliness, and high electrical conductivity. In this report, we synthesized molybdenum selenide ($Mo_{18}Se_{24}$) and magnesium molybdenum selenide ($Mg_3Mo_{18}Se_{24}$) (MoSe/MMSe) composite electrode materials on Ni foam (NF) *via* a facile hydrothermal technique. The MoSe/MMSe composite electrode exhibited superior areal capacity/specific capacity values of 1154.4 μA h cm^{-2}/250.9 mA h g^{-1} compared to individual electrodes. In addition, the effects of the single metal selenides MoSe and MgSe on the electrochemical properties were analyzed. Meanwhile, onion-derived activated carbon-coated NF (OAC/NF) was used as the negative electrode and exhibited high specific capacitance. Finally, a MoSe/MMSe/NF (positive (+))//OAC/NF (negative (−)) hybrid SC (HSC) cell was assembled. The HSC cell delivered maximum energy density of 28.5 W h kg^{-1}, maximum power density of 2353.8 W kg^{-1}, and long-term cycling stability of 74.3% after 45 000 cycles. Furthermore, the real-time practical applications of the HSC cell were tested by powering various electronic components.

1. Introduction

Owing to the energy crisis and natural disasters, it has become necessary to design and develop advanced energy storage conversion systems (ESSs). In addition, the rapid growth in science and technology has led to a huge demand for ESSs. Supercapacitors (SCs) are considered one of the most promising ESSs owing to their unique characteristics, including excellent cycling stability, environmental friendliness, high power density (P_d), and fast charging/discharging rate.[1–3] Generally, SCs are used in various commercial applications, such as flashlights, inverters, PC cards, and small media players. However, compared to batteries, SCs have some limitations, such as a low energy density (E_d) and potential window, which restrict the scope of their actual range of applications. According to the formula $E_d = 1/2CV^2$, where C denotes the capacitance and V denotes the potential window, there are two pathways to improve the E_d of SCs: increasing C and V. Generally, C depends on key parameters, such as surface area, electrical conductivity, and nanoarchitecture. Additionally, efficient handling of positive (+) and negative (−) electrode materials plays a key role in improving their electrochemical performance and voltage window.[4–6] For high-performance SCs, different electrode materials have been employed, for example, single transition metal oxides (NiO, RuO_2, Fe_2O_3, Co_3O_4, MnO_2, *etc.*), carbon-based materials (carbon nanotubes (CNTs), multi-walled CNTs, graphene, carbon dots, vapor-grown carbon fibers, *etc.*), conductive polymers (poly(3,4-ethylenedioxythiophene), polyaniline, *etc.*),[7,8] and transition metal selenides (single/bimetallic selenides of CoSe, NiSe, WSe_2, $MoSe_2$, $NiCo_2Se_4$, $CoFe_2Se_4$, $CoMoSe_4$, and $NiMoSe_4$). Among them, binary transition metal selenides (BTMSs) have been considered promising electrode materials for SC applications because of their rich redox states, chemical durability, and excellent electrical conductivity compared to single metal selenides and binary transition metal oxides.[9,10] Sulfur (S), oxygen (O), and selenium (Se) belong to group VI of the periodic table and exhibit similar properties. However, Se shows lower electronegativity/weaker binding compared to the S and O elements owing to its high electrical conductivity of 1×10^{-3} S m^{-1}.[9–12] Recent research has reported MoSe as an efficient electroactive electrode for SCs, batteries, and solar cells, and electrocatalytic water splitting, due to its exceptional electrical conductivity, structural properties, band-gap value, and high mechanical stability. Moreover, the Mo element exhibits variable oxidation states ranging from +2 to +6, low resistance value, and long interplane distance.[13,14] However,

---

Department of Electronics and Information Convergence Engineering, Institute for Wearable Convergence Electronics, Kyung Hee University, 1732 Deogyeong-daero, Giheung-gu, Yongin-si, Gyeonggi-do 17104, Republic of Korea. E-mail: jsyu@khu.ac.kr

† Electronic supplementary information (ESI) available. See DOI: https://doi.org/10.1039/d4ta01755b

the extensive application of MoSe is limited by its poor conductivity and serious aggregation in the fabrication process. On the other hand, Mg is a promising material for research owing to its low cost and environmental safety, and it has been widely used for hazardous waste chemical treatment, catalysis, refractory materials, plasma display panels, and superconductor applications. Additionally, Mg ions have a high negative standard potential (−2.375 V *vs.* RHE) and are more stable in pure electrolyte because of their superior conductivity and electrochemical activity. Additionally, Mg ions do not participate in reversible redox reactions; rather, they facilitate fast redox reactions in faradaic molybdenum elements. The results showed improvements in cycling stability, electron transfer capabilities, and electrochemical properties.[15] Our research work mainly focuses on preparing BTMS composites by combining MgSe and MoSe materials due to the synergistic effect of the two components, yielding high capacities, high-voltage windows, and good cycling stability. Generally, composite materials hold enormous potential to circumvent present limitations, such as better architecture design offering more durability, longer cycle life, higher energy density, higher power density, and better stability as well as environmental-friendliness to combat climate change.

So far, various works have reported composite BTMS electrode materials in SC applications. For example, Du *et al.* reported that (Ni, Co)Se_2/(Ni, Co)Se_2 delivered a high specific capacity of 220.34 mA h g^{-1} with 88.9% capacity retention after 5000 galvanostatic charge–discharge (GCD) cycles.[16] Nagaraju *et al.* synthesized a $Cu_{6.0}Se_{5.22}/Ni_{2.0}V_{4.0}Se_{8.0}$ electrode, exhibiting a high specific capacity of 94.4 mA h g^{-1} with good cycling retention of 103.8% after 8000 GCD cycles.[17] The $FeCoSe_2$@NiCo electrode prepared by L. Wan *et al.* revealed a high specific capacity of 220.9 mA h g^{-1} with 83.5% capacity retention after 5000 GCD cycles.[18] Muralee Gopi *et al.* reported that a $CoFe_2Se_4$@$CoNiSe_2$ electrode showed a high specific capacity of 183.4 mA h g^{-1} with a good cycling retention of 99.2% after 3000 GCD cycles.[19] W. Liu *et al.* reported that a MOF derived ZnO/C@(Ni, Co)Se_2 electrode displayed a high specific capacity of 164.18 mA h g^{-1} with a good cycling retention of 98.2% after 5000 GCD cycles.[20] Recently, our research group reported that a $Mo_{18}Se_{24}/Mg_3Mo_{18}Se_{24}$ (MoSe/MMSe) composite exhibited a high specific capacity of 250.9 mA h g^{-1} and 72.5% capacity retention after completing 50 000 GCD cycles.

To date, binder-free BTMS electrode materials have been prepared using various synthesis techniques, such as microwave-assisted process, sol–gel process, hydrothermal method, electrodeposition, and solvothermal process. Thus, several structures have been explored in the nanorange, such as spheres, belts, rods, wires, and flowers, which offer many advantages. However, combining different nanostructures to form a hybrid nanoarchitecture provides unique properties, such as high porosity, large surface area, more active sites, high mass diffusion, and fast charge-transport process.[21,22]

Biomass-derived activated carbon (AC)-based electrode materials are attracting increasing attention for negative electrode material in SC applications owing to their low cost, reduced toxicity, reproducibility, and abundance.[23–25] Biomass-derived ACs have been prepared using various sources such as mollusc shells, walnut shells, sugarcane, rice husks, coconut shells, and other biomass derivatives. The preparation of AC electrode materials involves several steps, including the identification of raw materials, carbonization at high temperatures, and initiation. Initiation is a crucial parameter for controlling the pore size and structure of carbon-based materials, and it affects their electrochemical and adsorption properties.[26] The combination of microporous and mesoporous structures provides increased space for electron transfer, faciliating the charge adsorption/desorption process through controlled diffusion and the molecular sieve effect. To date, AC-based electrode materials have exhibited specific capacitance (C_{sc}) values of 84, 250, and 172 F g^{-1}, respectively.[27,28] J. Wei *et al.* prepared bio-oil-derived hydrochar as an SC electrode material that exhibited a good C_{sc} value of 225.4 F g^{-1} at 1 A g^{-1}.[29] R. Kumari *et al.* prepared an AC-based SC derived from waste soybean oil with coffee ground additives which exhibited a good C_{sc} value of 70.97 F g^{-1} at 0.5 mA cm^{-2}.[30] Y. Li *et al.* converted jujube shell bio-waste into biomass-derived carbon for SC electrode materials, which showed a good C_{sc} value of 535.4 F g^{-1} at 1 A g^{-1}.[31] Onions are the most important vegetable, being the second most widely cultivated vegetable worldwide, resulting in massive consumption. But, 10% of onion products are discarded directly into the environment as waste. Using onion waste products to create AC is critical for the environment. Moreover, onion-derived ACs (OACs) contain carbon, N, and some heteroatoms, *e.g.*, S, B, N, and P, which makes them a beautiful raw material. According to the literature, N atoms exist in the binding of pyrrolic N, which enhances the electron transfer mechanism and faradaic redox-type energy storage. Meanwhile, O and S groups are primarily present in the binding states of the hydroxyl, carbonyl, and carboxyl functional groups and sulfite (SO_3^{2-})/thiol (>S) groups, respectively. The groups further enhance the faradaic redox type of energy storage.[50] Owing to these properties, OACs have been targeted as a negative electrode for SC applications.

In this study, a novel binder-free MoSe/MMSe material was prepared as a positive electrode *via* a facile hydrothermal method. The electrochemical properties of the synthesized composite MoSe/MMSe electrode materials were studied. Their electrochemical performances were compared with those of individual MoSe and MgSe electrode materials. OAC was used as the negative electrode. The OAC electrode showed higher C_{sc} values and good cycling stability. In addition, a hybrid SC (HSC) cell was fabricated using the MoSe/MMSe as a positive electrode and OAC as a negative electrode, respectively. The electrochemical performance of the HSC cell was evaluated. Real-time practical applications of the fabricated HSC were demonstrated by powering small-scale electronic devices.

2. Experimental procedure

In this experiment, the chemicals and materials were used without further purification during the entire synthesis procedure (ESI†); the detailed material and electrochemical characterizations are described in the ESI.†

2.1. Preparation of the MoSe/MMSe material

The MoSe/MMSe electrode material was synthesized using a one-pot hydrothermal technique on a nickel foam (NF) substrate. Initially, 0.25 g of magnesium nitrate hexahydrate ($Mg(NO_3)_2 \cdot 6H_2O$), 0.67 g of ammonium molybdate tetrahydrate ($(NH_4)_6Mo_7O_{24} \cdot 4H_2O$), 0.15 g of urea ($CO(NH_2)_2$), 0.12 g of ammonium fluoride (NH_4F), and 0.09 g of selenous acid (H_2SeO_3) were added into 80 mL deionized water (DIW) and stirred until they completely dissolved at room temperature. The NF substrate was washed with 1 M HCl solution to eliminate the nickel oxide layer and then washed with DIW and ethanol (EtOH), respectively, and it was dried in an oven at 90 °C for 12 h. Subsequently, an NF with a surface area of 1×1 cm^2 was attached to a glass slide and immersed in the above solution. The entire setup was then transferred to an autoclave and heated at 170 °C for 30 min. Once cooled down to room temperature, the NF samples were cleaned with DIW and EtOH. The sample was denoted as MoSe/MMSe and the mass-loading active material on the NF was measured to be ~4.6 mg cm^{-2}. Using the above process, MoSe and MgSe were synthesized to study the effect of single metal selenide on the overall electrochemical properties. The mass loadings of the MoSe and MgSe materials were determined to be 3 and 3.2 mg cm^{-2}, respectively.

2.2. Preparation of the OAC material

First, the outer layer of the onion was carefully separated from the smooth surface. The surface was carefully cleaned with DIW and EtOH to remove impurities. Subsequently, the onions were finely ground in a mixer grinder, and the obtained mixture was filtered using Whatman filter paper. Thereafter, the obtained pulp was dried in a hot oven at 90 °C for 24 h, and was later carbonized using a tube furnace under a nitrogen (N_2) atmosphere at a temperature of 800 °C with a ramp of 3 °C min^{-1} for 2 h. Following that, the obtained black powder was carefully washed with DIW and EtOH, respectively, and finally, the OAC material was obtained.

3. Results and discussion

A schematic representation of the fabrication procedure for the MoSe/MMSe composite material is shown in Fig. 1(a–c). The Mo, Mg, and Se sources were added to DIW (80 mL) and stirred until they were completely dissolved, as shown in Fig. 1(a). Subsequently, a facile, low-cost, and highly effective hydrothermal technique was used at a temperature of 170 °C to deposit the MoSe/MMSe composite material on the NF surface, as shown in Fig. 1(b). During the hydrothermal process, H_2SeO_3 releases Se^{2-} ions, $Mg(NO_3)_2 \cdot 6H_2O$ releases Mg^{2+} ions, $(NH_4)_6Mo_7O_{24} \cdot 4H_2O$ releases Mo^{4+}, Mo^{5+}, and Mo^{6+} ions, and the NF acts as a self-sacrificing template. Moreover, the porous NF conductor accelerates ion transport, whereas the developed active material provides a large surface area. Here, $CO(NH_2)_2$ and NH_4F acted as reducing and structure directing agents, respectively. Generally, hydrothermal techniques play key roles in the nucleation, phase growth, nanostructure formation, and particle size. First, the released Se^{2-} ions effectively interacted with Mg^{2+} ions and Mo^{4+}, Mo^{5+}, and Mo^{6+} ions, respectively. The formed MoSe/MMSe composite material is presented in Fig. 1(c). On the other hand, the AC was derived from the onion source and the dry pulps are shown in Fig. 1(d). To carbonize the sample, the obtained dried pulps were heated using a tube furnace at a temperature of 800 °C with a ramp of 3 °C min^{-1} for 2 h in a N_2 atmosphere, as shown in Fig. 1(e). The obtained powder was later carefully washed with DIW and EtOH, respectively and dried in an oven at 90 °C for 12 h. The obtained OAC electrode material is shown in Fig. 1(f).

The surface morphology of the prepared composite MoSe/MMSe material was observed using field-emission scanning electron microscope (FE-SEM), as shown in Fig. 2. At a low magnification, the FE-SEM image revealed a uniformly grown mixed nanoarchitecture on the NF surface, as shown in Fig. 2(a)(i). The mixed nanostructures fully cover the NF surface, as shown in Fig. 2(a)(ii). In addition, at a higher magnification, the nanoarchitecture containing nanospheres (NSs) and nanowire (NWs) could be clearly observed with an average size of ~100 nm (Fig. 2(a)(iii)). Herein, the NWs have several advantages, such as large surface area, which enables plenty of charge accommodation that can enhance the redox process. Besides, these NWs act as electron superhighways to supply the generated charge promptly to an external load. On the other hand, NSs may further increase the surface area of the entire material, which boosts the redox rate by offering numerous redox sites. The hierarchical connection of these NSs and NWs boosts charge transportation. Also, the nanosized gaps among them permit the electrolyte ions to diffuse, followed by the stimulation of the entire active material.[32,33] The FE-SEM images of the MoSe and MgSe materials are shown in Fig. S1 of the ESI.† The elemental distribution of the composite material was examined using energy-dispersive X-ray (EDX) spectroscopy, as shown in Fig. 2(b) and (c)(i–iii). The EDX spectrum of the MoSe/MMSe electrode represented the presence of different compositional elements, such as Mo, Mg, and Se. Besides, the elemental mapping and layered electronic images indicated the uniform presence of Mg, Mo, and Se elements throughout the resultant mixed morphology of the material. In addition, the inner morphological structure of the synthesized MoSe/MMSe electrode material was studied by using a transmission electron microscope (TEM). From the TEM images, the interconnected NS and NW morphologies could be observed, which is consistent with the FE-SEM results in Fig. 2(a)(i and iii). The TEM image revealed that the NS and NW morphologies were highly porous, as shown in Fig. 2(d and e). In addition, the TEM images of the MoSe/MMSe composite material displayed a good polycrystalline nature with the lattice spacings of 3.3 and 5.5 Å corresponding to the (11-4) and (330) planes of $Mo_{18}Se_{24}$ and $Mg_3Mo_{18}Se_{24}$ phases, respectively, as shown in Fig. 2(f)(i and ii). Furthermore, the selected area electron diffraction (SAED) pattern showed the polycrystalline nature of the prepared nanocomposite, as shown in the inset of Fig. 2(e). The TEM results confirmed the presence of both phases.[32,34] Using inductively coupled plasma spectroscopy (ICP) analysis, the metal elemental ratio of the prepared MoSe/MMSe composite

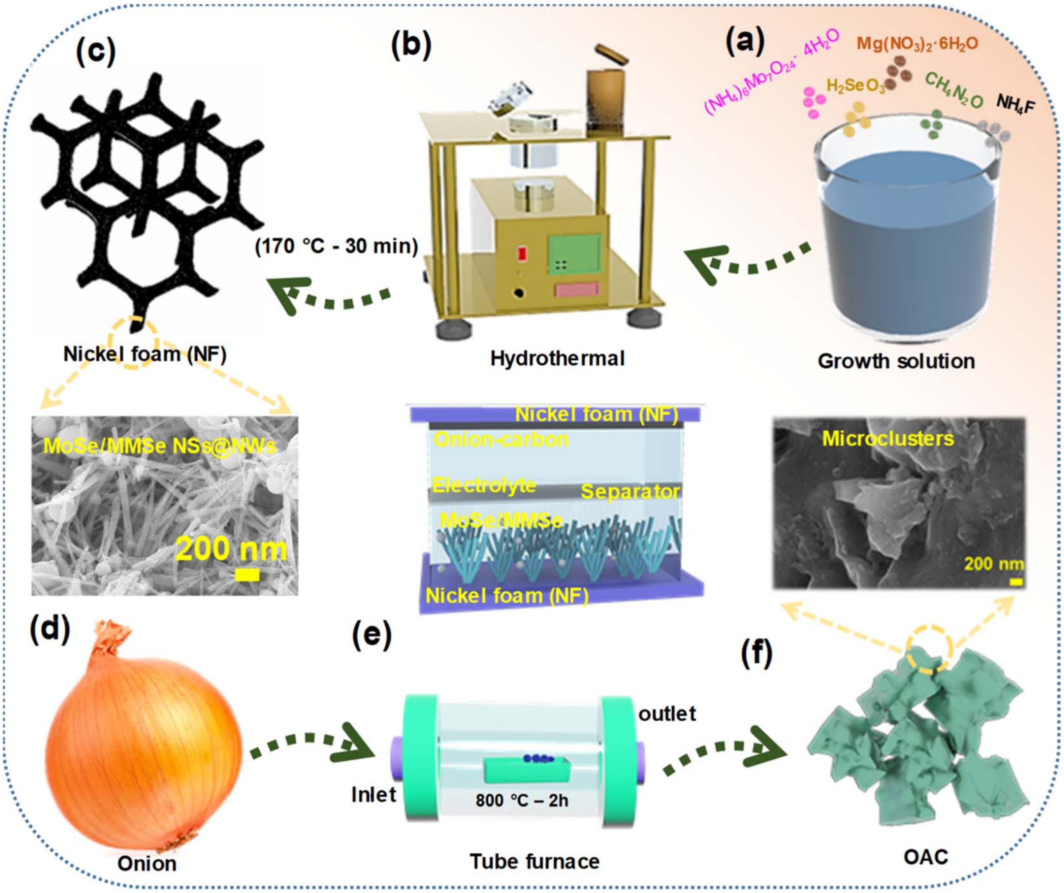

Fig. 1 Schematic representation for the fabrication procedure of the (a–c) MoSe/MMSe composite material and (d–f) OAC material.

material was investigated as shown in Fig. S2 of the ESI.† The crystallinity and phase composition of the as-prepared material were analyzed by X-ray diffraction (XRD), as shown in Fig. 2(g). From the XRD pattern, three high-intensity peaks were observed at the 2θ values of 44.1°, 51.5°, and 76.1°, which is well matched with the diffraction pattern of the bare NF substrate. Additionally, diffraction peaks were observed at the 2θ values of 49.9°, 55.9°, 57.9°, 59.4°, 60.8°, and 68.9° corresponding to the crystalline planes of (232), (330), (23-4), (24-2), (045), and (018), respectively in the $Mg_3Mo_{18}Se_{24}$ phase (JCPDS #96-433-8841). Moreover, other diffraction peaks were observed at the 2θ values of 30.1°, 33.2°, and 37.1°, corresponding to the crystallographic planes of (11-3), (11-4), and (220), respectively, in the $Mo_{18}Se_{24}$ phase (JCPDS #96-153-9631). Furthermore, the oxidation states/chemical compositions of the MoSe/MMSe composite material were examined by X-ray photoelectron spectroscopy (XPS) analysis. The total XPS survey scan spectrum verified the presence of Mg 1s, Mo 3d, and Se 3d elements, as shown in Fig. S4 of the ESI.† The core-level high-resolution (HR) XPS spectrum of Mg 1s is presented in Fig. 2(h) and it showed a single peak at the binding energy of 1305.8 eV, indicating the presence of Mg.[35,36] In the core-level spectrum of Mo 3d (Fig. 2(i)), the two peaks at 232.1 and 229.2 eV correspond to Mo $3d_{3/2}$ and Mo $3d_{5/2}$, respectively. Moreover, the Mo $3d_{3/2}$ and Mo $3d_{5/2}$ peaks were split into single peaks corresponding to the Mo^{4+} and Mo^{5+} oxidation states, respectively. The peak observed at 235.1 eV is related to MoO_x, and it revealed the Mo^{6+} oxidation state.[37,38] In addition, the core-level spectrum of the Se 3d is presented in Fig. 2(j), and two peaks were identified at 55.8 and 54.9 eV corresponding to Se $3d_{3/2}$ and Se $3d_{5/2}$, respectively, which indicates the Se^{2-} state.[39,40] These results confirmed the successful preparation of the MoSe/MMSe composite.

The electrochemical properties of the synthesized MoSe/MMSe, MoSe, and MgSe electrodes were investigated using Ivium software (IviumStat Technologies) in a three-electrode setup using a 1 M potassium hydroxide (KOH) solution as the electrolyte at room temperature, as shown in Fig. 3. Fig. 3(a) illustrates the cyclic voltammetry (CV) curves at 3 mV s^{-1} in a voltage window of 0.0–0.5 V. Here, the MoSe/MMSe composite electrode exhibited a larger CV response than the MoSe and MgSe electrodes. The composite electrode exhibits better charge storage properties owing to the advantages of the mixed nanostructures. Herein, all the CV profiles represent a pair of oxidation and reduction peaks, indicating faradaic-type reactions. For comparison, the GCD profiles of all the electrodes were tested within the voltage window of 0.0–0.5 V at 3 mA cm^{-1}, as shown in Fig. 3(b). The composite electrode exhibited longer charge/discharge times than the other electrodes, which agrees well with the CV results. The areal (C_A)/specific capacity (C_S) values were calculated from the GCD

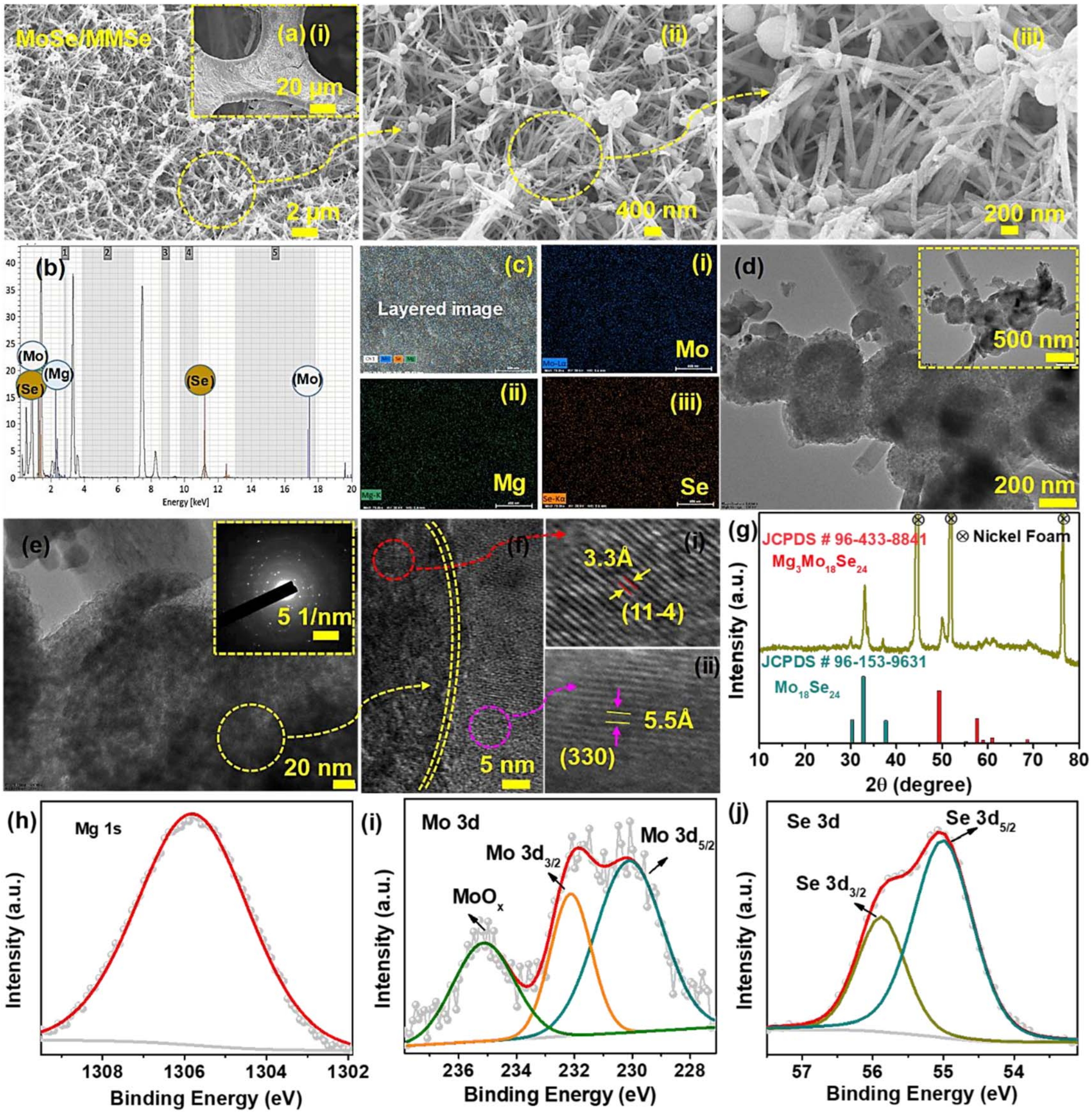

Fig. 2 (a)(i–iii) Low- and high-magnification FE-SEM images of the MoSe/MMSe composite material. (b) EDX spectrum and (c)(i–iii) elemental mapping images of the MoSe/MMSe composite material. (d) Low- and (e) high-magnification TEM images of the MoSe/MMSe composite material. The inset of (e) shows the corresponding SAED pattern. (f)(i and ii) Lattice fringes and (g) XRD pattern of the MoSe/MMSe composite material. HR XPS spectra of the (h) Mg 1s, (i) Mo 3d, and (j) Se 3d elements for the MoSe/MMSe composite material.

profiles using eqn (S1) and (S2) of the ESI.† The C_A/C_S values obtained for the MoSe/MMSe, MoSe, and MgSe electrodes were 1154.4 µA h cm^{-2}/250.9 mA h g^{-1}, 615 µAh cm^{-2}/192.4 mA h g^{-1}, and 520.1 µAh cm^{-2}/173.3 mA h g^{-1}, respectively (Fig. 3(c)). A mixed nanostructure containing NSs and NWs could be advantageous for achieving large ion-accessible surface area and rapid charge transport. However, active materials with a mixture of these nanostructures would further enhance the charge storage performance owing to their respective structural properties. Moreover, the charge transfer kinetics were studied by electrochemical impedance spectroscopy (EIS) analysis within the frequency range from 0.01 Hz to 100 kHz, as shown in Fig. 3(d). The EIS plot of the electrode includes a semicircular arc and straight line in the high- and low-frequency regions, respectively. The MoSe/MMSe composite electrode revealed lower solution resistance (R_s) and charge-transfer resistance (R_{ct}) values, compared to the other two electrodes (MoSe and MgSe), of ~0.98 Ω and ~3.98 Ω, respectively. Here, a lower R_{ct} value represents a fast electrolyte interface between the electrode and electrolyte, ultimately showing high capacity values. For the MoSe electrode, the R_s and R_{ct} values were found to be ~1.94 Ω and ~4.29 Ω, respectively. Similarly, the R_s and R_{ct} values of the MgSe electrode were ~2.1 Ω and ~6.09 Ω, respectively. Additionally, the CV curves of the MoSe/MMSe composite electrode were tested within a voltage window of 0–0.5 V at various scan rates ranging from 3 to 30 mV s^{-1}. All the CV profiles showed faradaic behavior. When the scan rate was increased, the area under the CV curve also increased, and the oxidation and reduction peaks shifted toward the positive and negative sides, respectively, indicating

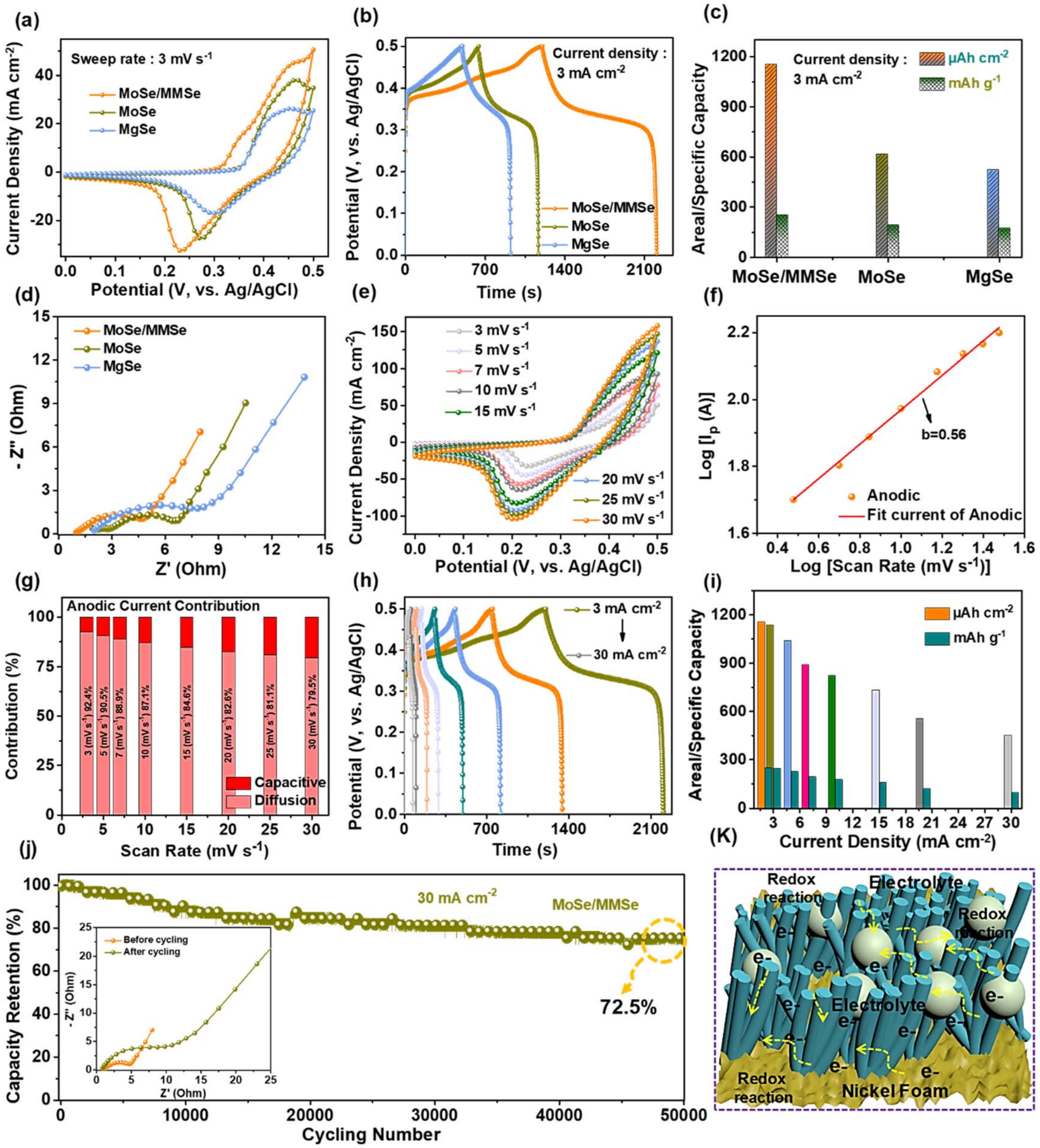

Fig. 3 Comparative (a) CV curves, (b) GCD curves, (c) C_A/C_s values, and (d) EIS plots of the MoSe/MMSe, MoSe, and MgSe electrodes. (e) CV curves at 3 to 30 mV s^{-1}, (f) *b* value and (g) current contribution percentage at different scan rates, (h) GCD curves, (i) C_A/C_s values, and (j) cycling stability test results of the MoSe/MMSe electrode. The inset of (j) shows the EIS plots of the MoSe/MMSe electrode before and after the cycling test. (k) Structural merits for the MoSe/MMSe electrode material.

a reversible faradaic reaction (Fig. 3(e)). The redox reactions occurring between $Mo^{4+}/Mo^{5+}/Mo^{6+}$, Mg/Mg^{2+}, Se^{2-} and the alkaline electrolyte are represented by the following equations:[41,42]

$$Mo_{18}Se_{24} + OH^- \leftrightarrow Mo_{18}Se_{24}OH + e^- \tag{1}$$

$$Mg_3Mo_{18}Se_{24} + OH^- \leftrightarrow Mg_3Mo_{18}Se_{24}OH + e^- \tag{2}$$

In addition, from the CV curve of the MoSe/MMSe composite electrode, the electrochemical behavior was studied using the following power law:[43]

$$i_p = av^b \tag{3}$$

where i_p denotes the peak current, which is related to the scan rate (v). Here, a and b signify variable factors after linear fitting. Generally, b indicates the energy storage kinetic behavior of the electrode. When $b = 1$ and 0.5, the electrode exhibited surface- and diffusion-controlled processes, respectively. From the fitting, the MoSe/MMSe composite electrode exhibits $b = 0.56$, which indicates a mixed charge storage mechanism for the pseudocapacitance and battery properties of the prepared electrode, as presented in Fig. 3(f). Moreover, the capacitive- and diffusion-controlled contribution percentages (%) of the

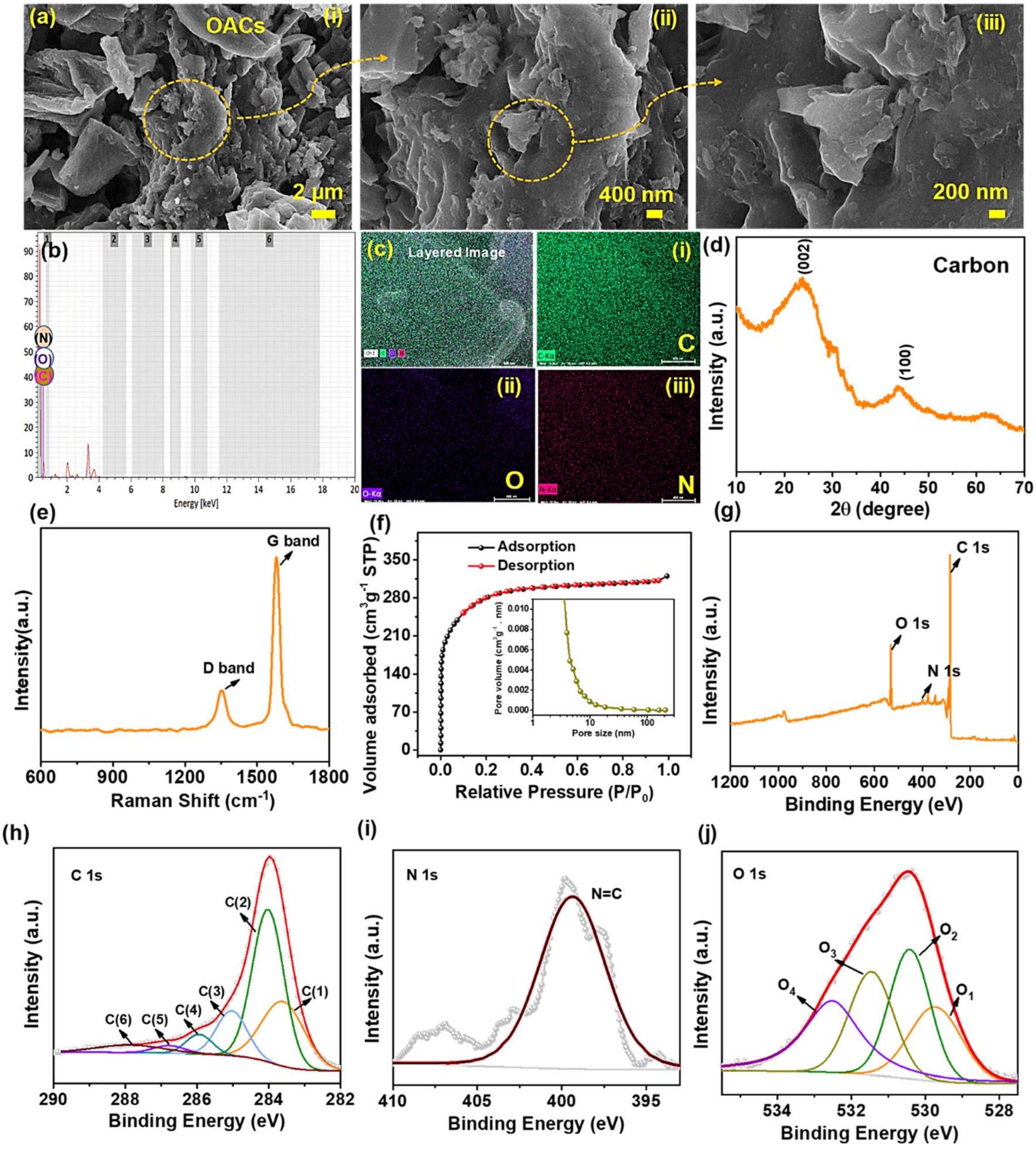

Fig. 4 (a)(i–iii) Low- and high-magnification FE-SEM images of the OAC material. (b) EDX spectrum and (c) (i–iii) elemental mapping images of the OAC material. (d) XRD pattern of the OAC material. (e) HR Raman spectrum of the OAC material. (f) N_2 adsorption and desorption isotherms of the prepared OAC material. (g) Total XPS survey scan spectrum and HR XPS spectra of the (h) C 1s, (i) N 1s, and (j) O 1s elements for the OAC material.

MoSe/MMSe composite electrode were calculated using the CV profiles from a modified equation:[44]

$$i_p = k_1 v + k_2 v^{1/2} \tag{4}$$

Here, i_p is the peak current and k_1 and k_2 refer the slope values. In addition, the $v^{1/2}$ and $i/v^{1/2}$ values were obtained from the fitted lines. The obtained diffusion-controlled contribution percentage values were 92.4%, 90.5%, 88.9%, 87.1%, 84.6%, 82.6%, 81.1%, and 79.5% at 3, 5, 7, 10, 15, 20, 25, and 30 mV s^{-1}, respectively, as shown in Fig. 3(g). The GCD curves of the MoSe/MMSe electrode were measured at various current densities ranging from 3 to 30 mA cm^{-2}. The GCD profiles demonstrate diffusion contribution behavior and are highly reversible, as shown in Fig. 3(h). Furthermore, from the GCD profiles, the C_A/C_S values were calculated and the resulting values are plotted in Fig. 3(i). The MoSe/MMSe composite electrode showed the C_A/C_S values of 1154.4 µA h cm^{-2}/250.9 mA h g^{-1} and 540.1 µAh cm^{-2}/98.5 mA h g^{-1} at 3 and 30 mA cm^{-2}, respectively. The pore size and surface area of the prepared MoSe/MMSe, MoSe, and MgSe composite materials were analyzed using Brunauer–Emmett–Teller (BET) and Barrett–Joyner–Halenda (BJH) techniques, as shown in Fig. S3 of the ESI.† In addition, the cycling stability is a vital parameter for the practical application of SCs. The cycling stability test of the MoSe/MMSe composite electrode was verified using continuous GCD cycles at 30 mA cm^{-2}, as seen in Fig. 3(j). During the cycling test, the MoSe/MMSe composite electrode exhibited a capacity retention of 72.5% after 50 000 GCD cycles. The EIS plots before and after the cycling test are shown in the inset of Fig. 3(j). The R_s/R_{ct} values before and after the cycling test were determined to be ∼0.98 Ω/∼3.98 Ω and ∼0.81 Ω/∼10.9 Ω, respectively. Moreover, as shown in Fig. 3(k), the prepared MoSe/MMSe composite electrode exhibited good electrochemical properties owing to the mixed nanostructures of NSs and NWs. The resultant nanoarchitecture provides large surface area, high porosity, and numerous active sites at the electrode–electrolyte interface. Consequently, this structure offers high electrical conductivity, electrochemical reactions, and structural durability. The CV and GCD profiles, and C_A/C_s values of the MoSe and MgSe electrodes are shown in Fig. S5 of the ESI.† The EDX spectrum of the MoSe/MMSe composite electrode after cycling is shown in Fig. S6 of the ESI.†

The OAC material was fabricated as the negative electrode, and its material properties are shown in Fig. 4. The morphology of the prepared OAC material was examined using FE-SEM. The low- and high-magnification FE-SEM images shown in Fig. 4(a)(i–iii) revealed the uniform structure of the clusters. From the high-magnification images, it is evident that the micro-sized bulk clusters contain extremely small nanoparticles. The porous structures of the OAC provide a large surface area and offer several active sites at the electrode/electrolyte interface, resulting in improved capacitance properties. The EDX spectra and elemental mapping images are shown in Fig. 4(b) and (c)(i–iii), respectively. These results confirmed the presence of C, N, and O in the OAC sample. The crystallinity and phase of the OAC material were analyzed using XRD technique (Fig. 4(d)). Two diffraction peaks occurred at the 2θ values of 24.5° and 43.7° corresponding to the crystallographic planes of (002) and (100), respectively. The broad peak at 24.5° is matched well with the (002) plane of the carbon material, which was identified as the parallel stacking of the carbon layer and the crystallographic plane of graphitic crystallites. In addition, the peak at 43.70° corresponds to the (100) plane, suggesting the existence of a honeycomb-like structure formed by sp^2 hybridized carbon atoms. The HR Raman spectrum of the OAC material is shown in Fig. 4(e). Two peaks were identified at 1352.1 and 1584 cm^{-1} and named peaks D and G which correspond to defect carbon and graphitic carbon, respectively. Moreover, the specific surface area (SSA) of the prepared OAC material was evaluated using BET, while the pore size distribution was determined by BJH analysis as shown in Fig. 4(f). The electrochemical properties mainly depended on its SSA and porous structure. The OAC powder was analyzed using N_2 adsorption–desorption measurements. The resultant adsorption isotherms of the OAC powder belong to the combination of type I and type IV isotherms according to the IUPAC classification. This indicates the existence of both microporous and mesoporous structures in the OAC powder, as shown in Fig. 4(f). The OAC powder sample exhibited a high BET SSA value of 617 m^2 g^{-1}. Furthermore, the pore size distribution calculated by the BJH indicates that a major peak was noticed at 4.2 nm in the OAC powder, as shown in the inset of Fig. 4(f). The surface of both microporous and mesoporous structures of the carbon material favors charge accommodation and good intercalation, which in turn results in better electrochemical

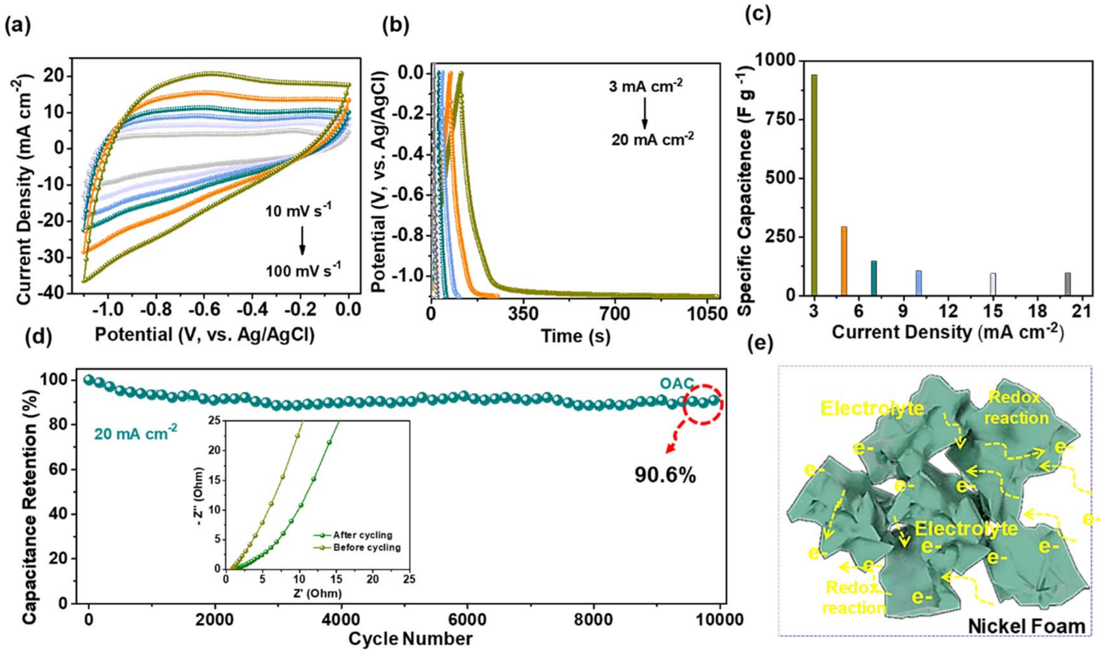

Fig. 5 Comparative (a) CV curves, (b) GCD curves, and (c) C_{sc} values of the OAC electrode. (d) Cycling stability test result of the OAC electrode. The inset of (d) shows the EIS plots of the OAC electrode before and after the cycling test. (e) Structural merits for the OAC/NF electrode material.

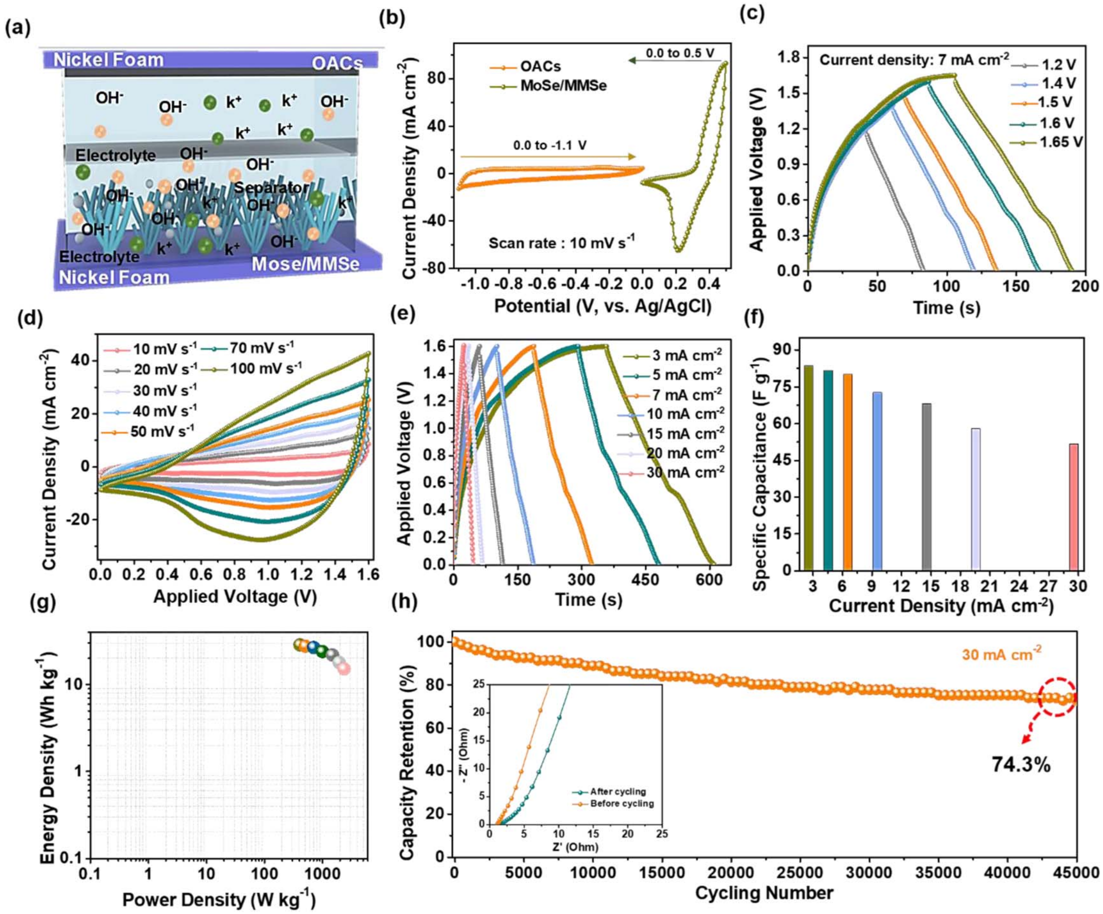

Fig. 6 (a) Schematic diagram of the HSC cell. (b) CV and GCD curves with reference to the potential windows for the MoSe/MMSe composite and the OAC electrodes. (c) GCD curves at different voltages. (d) CV curves at different scan rates and (e) GCD curves at various current densities, (f) C_{sc} values, (g) Ragone plot, and (h) cycling stability results for the HSC cell. The inset of (h) shows the EIS plots of the HSC cell before and after the cycling test.

activity.[45,46] Fig. 4(g–j) show the XPS spectra of the OAC sample. The total XPS survey scan spectrum confirmed the presence of C 1s, N 1s, and O 1s, as shown in Fig. 4(g). In Fig. 4(h), the core-level HR XPS spectrum of the C 1s contained six peaks at 283.8, 284.1, 285.1, 286.1, 287.1, and 288.1 eV, which are related to carbide carbon, C═C, C–C, C–O, C═O, and O–C═O bonds, respectively.[47,48] In the HR XPS spectrum of N 1s (Fig. 4(i)), a peak at 400.1 eV was observed, indicating the presence of N═C bonds.[49,50] The core-level O 1s spectrum contains four peaks: O_1 (529.7 eV), O_2 (530.2 eV), O_3 (531.4 eV), and O_4 (532.5 eV), which are associated with M–O bonds, oxygen species, and C═O and C–O–C bonds, respectively, as shown in Fig. 4(j).[34] These characterizations indicate that the OAC material was successfully synthesized.

The slurry preparation process for the OAC/NF electrode is presented in the ESI,† and the CV, GCD, and EIS plots of the OAC electrode are shown in Fig. 5(a–c). The CV profiles are tested within the applied voltage window of 0.0 to −1.1 V at different scan rates ranging from 10 to 100 mV s^{-1}, representing rectangular shapes that indicate the electrical double-layer capacitor behavior. When the scan rate increased, the resultant current response increased, as shown in Fig. 5(a). Besides, Fig. 5(b) shows the GCD curves of the OAC electrode measured at various current densities ranging from 3 to 20 mA cm^{-2}. The GCD profiles exhibited a symmetric triangular shape, suggesting good coulombic efficiency and reversibility. The C_{sc} values were calculated from the GCD profiles using eqn (S3) in the ESI;† the resulting values are shown in Fig. 5(c). An C_{sc} value of 940.6 F g^{-1} was obtained at 3 mA cm^{-2}, which decreased to 97.1 F g^{-1} at 20 mA cm^{-2}, indicating good electrochemical performance. Moreover, the electrochemical properties of our OAC electrode material were compared with those of some recently reported biomass-derived SC electrode materials as shown in Table S1 of the ESI.† The stability test was conducted at 20 mA cm^{-2} in repeated continuous GCD processes, and the OAC electrode showed a good capacitance retention of 90.6% after 10 000 GCD cycles, as shown in Fig. 5(d). The inset of Fig. 5(d) shows the EIS analysis of the OAC electrode before and after the stability test to study the impedance behavior. From the EIS plot before and after the cycling test, the obtained R_s values were 1.52 Ω and 0.81 Ω, respectively. Similarly, the R_{ct} values were observed to be 0.39 Ω and 0.23 Ω, respectively. The figure of merit for the OAC/NF electrode is shown in Fig. 5(e). The porous structure provides numerous active sites for the electrode/

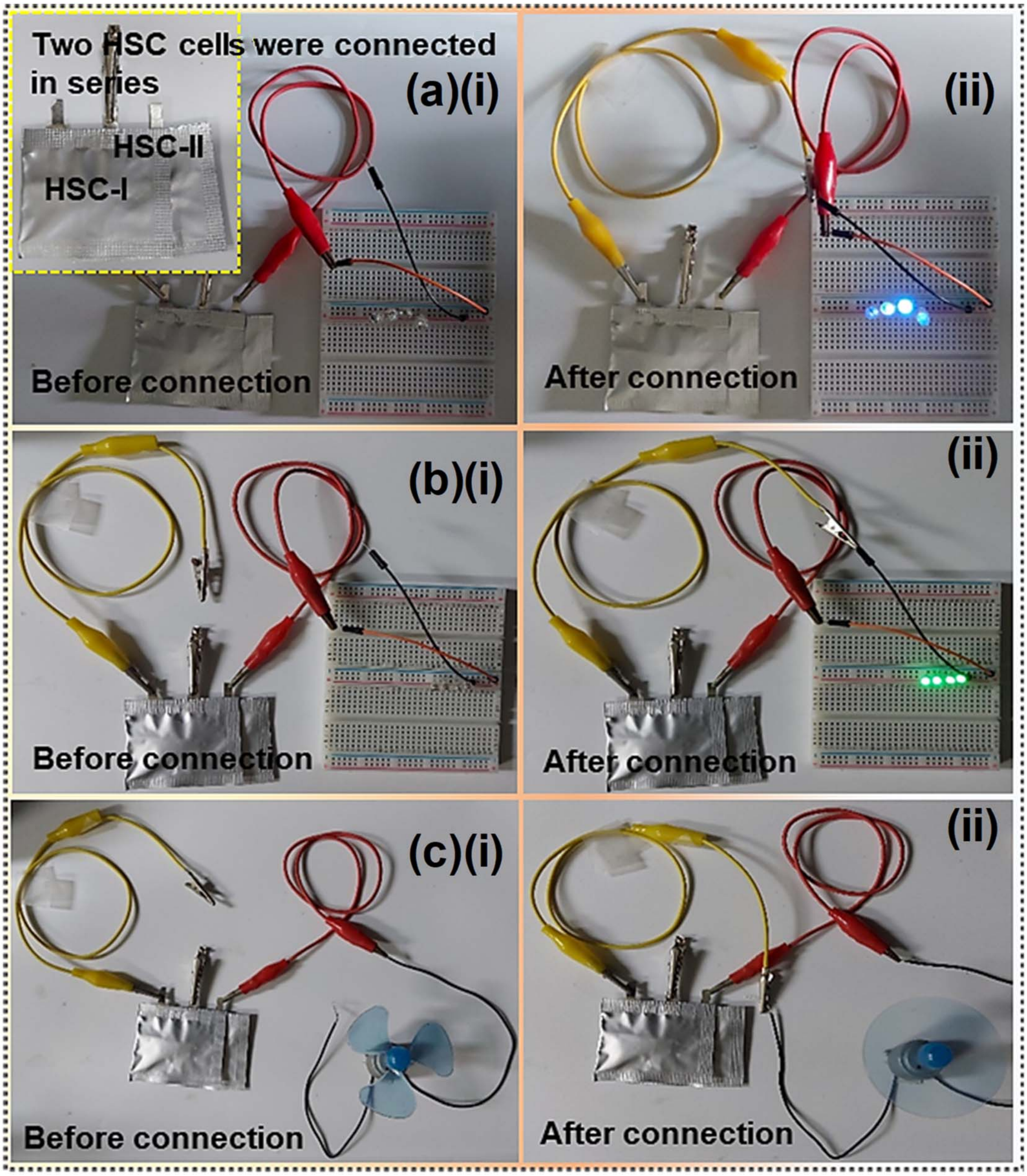

Fig. 7 Photographic images of the two HSC cells connected in series connection to the (a)(i and ii) blue LEDs and (b)(i and ii) green LEDs. The insets of (a)(i) show the photographic images of the two fabricated HCS cells. (c)(i and ii) Photographic images of the two HSC cells connected in series to the toy-type DC motor fan.

electrolyte interface, resulting in improved electrochemical properties. Upon completion of the cycling stability test, the EDX spectrum analyses of the OAC electrode are presented in Fig. S7 of the ESI.†

To test the practical applications of the prepared electrodes, a MoSe/MMSe/NF (+)//OAC/NF (−) HSC cell was assembled using MoSe/MMSe as the positive electrode and OAC as the negative electrode, as shown in Fig. 6(a). Initially, a pouch-type cell was fabricated using an aluminum pouch, and a few drops of 1 M KOH electrolyte were added to this setup. The HSC cell was then tightly sealed using a sealer to prevent electrolyte leakage and impurities. Whatman filter paper was used to avoid a short circuit between the positive and negative electrodes, and Ni tabs were used as conductive terminals. Before assembly, the HSC cell was mass-balanced using eqn (S6) of the ESI.† Fig. 6(b) shows the comparative study of the CV profiles for the prepared MoSe/MMSe/NF (+) and OAC/NF (−) electrodes at a fixed scan rate of 10 mV s^{-1} within the potential range of 0–0.5 and 0–1.1 V, respectively, tested in a three-electrode setup. From the above the CV profiles, the assembled HSC cell may tolerate a voltage window of 0 to 1.6 V. To provide evidence to the statement, the GCD profiles were tested at different voltage windows from 1.0 to 1.65 V at a fixed current density of 7 mA cm^{-2} and the resultant GCD profiles are presented in Fig. 6(c). In the applied voltage window of 0–1.65 V, the GCD curves show a slight deviation owing to H_2/O_2 evolution. For this reason, the voltage window of the HSC cell was set to 1.6 V for further analysis. As shown in Fig. 6(d and e), the CV and GCD profiles of the HSC were measured at different scan rates and current densities, ranging from 10 to 100 mV s^{-1} and 3 to 30 mA cm^{-2}, respectively. All the CV and GCD profiles exhibited both capacitive and redox behaviors at each scan rate owing to the good mass balancing of both electrodes. Moreover, the CV and GCD profiles of the HSC cell were maintained even at high scan rates and current densities of 100 mV s^{-1} and 30 mA cm^{-2}, respectively, indicating a decent capacitive nature and exceptional electrochemical properties. Moreover, the C_{SC} values of the HSC cell were 83.5, 81.5, 79.9, 72.6, 68.1, 58.1, and 51.7 F g^{-1} at current densities of 3, 5, 7, 10, 15, 20, and 30 mA cm^{-2}, respectively as shown in Fig. 6(f). The E_d and P_d values of the HSC were calculated using eqn. (S4) and (S5) provided in the ESI† and are marked in the Ragone plot (Fig. 6(g)). The HSC cell revealed maximum E_d and P_d values of 28.5 W h kg^{-1} and 2353.8 W kg^{-1}, respectively. Moreover, the E_d and P_d values of the HSC were compared with those previously reported, as presented in Table S2 of the ESI.† In Fig. 6(h), the cycling stability test of the HSC cell was performed by repeated GCD processes at 20 mA cm^{-1}, exhibiting a capacitance retention of 74.3% after long-term cycling for 45 000 GCD cycles. The EIS plots before and after the cycling test are presented in the inset of Fig. 6(h). From the EIS plots, the R_s values were 1.06 Ω and 1.29 Ω before and after the cycling test, respectively and the R_{ct} values were estimated to be 0.58 Ω and 0.95 Ω, respectively.

Finally, the commercial applicability of the fabricated HSC cell was verified by powering it with various electronic components, as shown in Fig. 7. Herein, two HSCs were connected in series to extend the applied voltage window, and a photographic image is displayed in the inset of Fig. 7(a). Photographic images of the blue and green light-emitting diodes (LEDs), before and after connections, are shown in Fig. 7(a)(i, ii) and (b)(i and ii), respectively. The blue and green LEDs were powered for approximately 3 min. Photographic images of a toy-type direct current (DC) motor fan are shown in Fig. 7(c)(i and ii). The DC motor fan was operated for 1 min.

4. Conclusion

In summary, we successfully synthesized a MoSe/MMSe composite electrode material with mixed nanostructures *via* the one-pot hydrothermal method. The composite electrode exhibited higher C_A/C_S values of 1154.4 μAh cm^{-2}/250.9 mA h g^{-1} compared to the individual metal selenide electrodes (MoSe and MgSe). This is due to the advantages of the prepared nanoarchitecture, including a large surface area, highly reversible redox reactions, and a fast transport rate. Moreover, the cycling stability test of the composite electrode was performed at 30 mA cm^{-2} and the result showed a long-term cycling stability of over 50 000 GCD cycles. Additionally, the effects of single metals on electrochemical properties were studied. On the other hand, the OAC/NF material was used as the negative electrode, which was found to have a high C_{sc} value of 940.6 F g^{-1}, exhibiting excellent cycling stability with a good capacitance retention of 90.6% at the end of 10 000 GCD cycles. Finally, a MoSe/MMSe/NF (+)//OAC/NF (−) HSC cell was fabricated, which demonstrated a good C_{sc} value of 83.5 F g^{-1} at 3 mA cm^{-2} with a long-term cycling stability at 30 mA cm^{-2}. The HSC cell showed maximum E_d and P_d values of 28.5 W h kg^{-1} and 2353.8 W kg^{-1}, respectively. Additionally, the real-time practical applications of the HSC cell were tested by powering various electronic components. Based on these results, the proposed binder-free MoSe/MMSe composite and OAC electrode materials are expected to serve as potential electrodes for advanced energy storage applications.

Conflicts of interest

There are no conflicts to declare.

Acknowledgements

This work was supported by the National Research Foundation of Korea (NRF) grant funded by the Korean government (MSIP) (No. 2018R1A6A1A03025708).

References

1 P. S. Shukla, A. Agrawal, A. Gaur and G. D. Varma, *J. Energy Storage*, 2023, **59**, 106580.
2 N. Chaudhary and M. Khanuja, *Energy Fuels*, 2022, **36**, 1034–1042.
3 Z. Shi, Y. Liu, Y. Zhang, J. Sun, J. Zheng, C. Wei, W. Du, L. Liu and C. Cheng, *J. Energy Storage*, 2023, **611**, 155758.
4 V. Sharma, S. J. Kim, N. H. Kim and J. H. Lee, *Chem. Eng. J.*, 2021, **415**, 128188.
5 X. Feng, Y. Huang, C. Li, Y. Xiao, X. Chen, X. Gao and C. Chen, *Electrochim. Acta*, 2019, **308**, 142–149.
6 G. Saeed, P. Bandyopadhyay, S. Kumar, N. H. Kim and J. H. Lee, *ACS Appl. Mater. Interfaces*, 2020, **12**, 47377–47388.
7 J. Barqi, S. M. Masoudpanah, M. Hasheminiasari and X. Liu, *J. Alloys Compd.*, 2023, **930**, 167509.
8 M. A. Yewale, R. A. Kadam, N. K. Kaushik, J. R. Koduru, N. B. Velhal, U. T. Nakate, A. A. Jadhavar, N. D. Sali and D. K. Shin, *Mater. Sci. Eng., B*, 2023, **287**, 116072.
9 Z. Jiang, Y. Wang, S. Yuan, L. Shi, N. Wang, J. Xiong, W. Lai, X. Wang, F. Kang, W. Lin, C. P. Wong and C. Yang, *Adv. Funct. Mater.*, 2019, **29**, 1807116.
10 Q. Huang, W. Su, G. Zhong, K. Xu and C. Yang, *Chem. Eng. J.*, 2023, **460**, 141875.
11 C. Wang, G. Sui, D. Guo, J. Li, W. Guo and D.-F. Chai, *J. Energy Storage*, 2022, **50**, 104714.
12 X. Qu, S. Jeon, J. Jeong, W. Kang, B. Xing, C. Zhang and S. W. Hong, *J. Alloys Compd.*, 2023, **966**, 171421.
13 M. Norouzibazaz, M. B. Gholivand, A. A. Taherpour and M. Mirzaei, *Mater. Today Energy*, 2023, **38**, 101447.
14 H. Peng, C. Wei, K. Wang, T. Meng, G. Ma, Z. Lei and X. Gong, *ACS Appl. Mater. Interfaces*, 2017, **9**, 17067–17075.
15 K. Karthikeyan, S. Amaresh, V. Aravindan and Y. S. Lee, *J. Mater. Chem. A*, 2013, **1**, 4105–4111.
16 M. Du, W. Xia, Z. Jiao, Y. Chen, M. Demir, Y. Zhang, M. Gu, X. Zhang and C. Wang, *J. Alloys Compd.*, 2023, **930**, 167459.

17 M. Nagaraju, B. Ramulu, S. J. Arbaz and J. S. Yu, *Appl. Surf. Sci.*, 2023, **622**, 156952.

18 L. Wan, L. Chen, M. Xie, J. Chen, Y. Zhang and C. Du, *J. Alloys Compd.*, 2022, **901**, 163567.

19 C. V. V. Muralee Gopi, A. E. Reddy and H.-J. Kim, *J. Mater. Chem. A*, 2018, **6**, 7439–7448.

20 W. Liu, F. Zhu, B. Ge, L. Sun, Y. Liu and W. Shi, *Chem. Eng. J.*, 2022, **427**, 130788.

21 M. Nagaraju, S. Chandra Sekhar, B. Ramulu, S. J. Arbaz and J. S. Yu, *J. Magnesium Alloys*, 2022, **10**, 3565–3575.

22 M. H. Aziz, A. Khan, H. M. Fahad, F. Shaheen, R. Ahmad, K. Mehboob and Q. Huang, *J. Energy Storage*, 2023, **63**, 106982.

23 R. Mehdi, S. R. Naqvi, A. H. Khoja and R. Hussain, *Fuel*, 2023, **348**, 128529.

24 X. Wang and G. Shi, *Energy Environ. Sci.*, 2015, **8**, 790–823.

25 Y. Xu, Z. Lin, X. Huang, Y. Liu, Y. Huang and X. Duan, *ACS Nano*, 2013, **7**, 4042–4049.

26 S. J. Rajasekaran, A. N. Grace, G. Jacob, A. Alodhayb, S. Pandiaraj and V. Raghavan, *Catalysts*, 2023, **13**, 286.

27 E. G. Shankar, A. K. Das and J. S. Yu, *J. Mater. Sci. Technol.*, 2022, **125**, 118–127.

28 W. Chen, H. Wang, W. Lan, D. Li, A. Zhang and C. Liu, *Ind. Crops Prod.*, 2021, **170**, 113700.

29 J. Wei, J. Sun, D. Xu, L. Shi, M. Wang, B. Li, X. Song, S. Zhang and H. Zhang, *Int. J. Environ. Res. Public Health*, 2023, **20**, 1355.

30 R. Kumari, V. Singh and C. Ravi Kant, *Mater. Chem. Phys.*, 2023, **305**, 127882.

31 Y. Li and B. Qi, *Electrochem. Commun.*, 2023, **152**, 107512.

32 S. C. Sekhar, B. Ramulu, M. H. Han, S. J. Arbaz, M. Nagaraju, H.-S. Oh and J. S. Yu, *Adv. Sci.*, 2022, **9**, 2104877.

33 S. A. Beknalkar, A. M. Teli, S. M. Mane, R. P. Dhavale, M. A. Yewale and J. C. Shin, *J. Energy Storage*, 2024, **76**, 109839.

34 M. Nagaraju, B. Ramulu, S. J. Arbaz and J. S. Yu, *J. Alloys Compd.*, 2023, **947**, 169490.

35 Y. Guo, Z. Gong, C. Li, B. Gao, P. Li, X. Wang, B. Zhang and X. Li, *Chem. Eng. J.*, 2020, **392**, 123682.

36 E. G. Shankar, A. K. Das and J. S. Yu, *Int. J. Energy Res.*, 2022, **46**, 1593–1608.

37 J. Baltrusaitis, B. Mendoza-Sanchez, V. Fernandez, R. Veenstra, N. Dukstiene, A. Roberts and N. Fairley, *Appl. Surf. Sci.*, 2015, **326**, 151–161.

38 S. Santhosh, A. K. Nanda Kumar, J. Kennedy and B. Subramanian, *Electrochim. Acta*, 2020, **354**, 136745.

39 H. Liu, H. Guo, N. Wu, W. Yao, R. Xue, M. Wang and W. Yang, *J. Alloys Compd.*, 2021, **856**, 156535.

40 D. Khalafallah, J. Miao, M. Zhi and Z. Hong, *Appl. Surf. Sci.*, 2021, **564**, 150449.

41 E. Levi, E. Lancry, A. Mitelman, D. Aurbach, O. Isnard and D. Djurado, *Chem. Mater.*, 2006, **18**, 3705–3714.

42 Z.-H. Tang, H.-Y. Zeng, K. Zhang, Z. Li, W. Yan, H.-B. Wang and H.-l. Yue, *Electrochim. Acta*, 2023, **468**, 143156.

43 M. Nagaraju, B. Ramulu, E. Girija Shankar and J. Su Yu, *Appl. Surf. Sci.*, 2023, **640**, 158339.

44 C. Wang, G. Sui, D. Guo, J. Li, X. Ma, Y. Zhuang and D.-F. Chai, *J. Energy Storage*, 2022, **50**, 104280.

45 Z. A. ALOthman, *Materials*, 2012, **5**, 2874–2902.

46 N. Mojoudi, N. Mirghaffari, M. Soleimani, H. Shariatmadari, C. Belver and J. Bedia, *Sci. Rep.*, 2019, **9**, 19352.

47 J. Kim, J. Chun, S.-G. Kim, H. Ahn and K. C. Roh, *J. Electrochem. Sci. Technol.*, 2017, **8**, 338–343.

48 M. K. Rybarczyk, K. Cysewska, R. Yuksel and M. Lieder, *Nanomaterials*, 2022, **12**, 1162.

49 W. Zhu, D. Shen and H. Xie, *J. Energy Storage*, 2023, **60**, 106595.

50 E. G. Shankar, A. K. Das and J. S. Yu, *J. Mater. Sci. Technol.*, 2022, **125**, 118–127.